

Ultrasmall Semiconducting Polymer Dots with Rapid Clearance for Second Near-Infrared Photoacoustic Imaging and Photothermal Cancer Therapy

Xiaoju Men, Fei Wang, Haobin Chen, Yubin Liu, Xiaoxiao Men, Ye Yuan, Zhe Zhang, Duyang Gao, Changfeng Wu, and Zhen Yuan*

Phototheranostic agents in the second near-infrared (NIR-II) window (1000–1700 nm) are emerging as a promising theranostic platform for precision medicine due to enhanced penetration depth and minimized tissue exposure. The development of metabolizable NIR-II nanoagents for imaging-guided therapy are essential for noninvasive disease diagnosis and precise ablation of tumors. Herein, metabolizable highly absorbing NIR-II conjugated polymer dots (Pdots) are reported for the first time for photoacoustic imaging guided photothermal therapy (PTT). The unique design of low-bandgap D-A π -conjugated polymer (DPP-BTzTD) together with modified nanoreprecipitation conditions allows to fabricate NIR-II absorbing Pdots with ultrasmall (4 nm) particle size. Extensive experimental tests demonstrate that the constructed Pdots exhibit good biocompatibility, excellent photostability, bright photoacoustic signals, and high photothermal conversion efficiency (53%). In addition, upon tail-vein intravenous injection of tumor-bearing mice, Pdots also show high-efficient tumor ablation capability with rapid excretion from the body. In particular, both *in vitro* and *in vivo* assays indicate that the Pdots possess remarkable PTT performance under irradiation with a 1064 nm laser with 0.5 W cm^{-2} , which is much lower than its maximum permissible exposure limit of 1 W cm^{-2} . This pilot study thus paves a novel avenue for the development of organic semiconducting nanoagents for future clinical translation.

1. Introduction

Theranostic nanoagents, which incorporate diagnostic and therapeutic capability, have emerged as a promising nanotechnology for cancer detection and treatment. As a multifunctional and all-in-one or one-for-all tool, theranostic nanoagents can provide more comprehensive information for diagnosing and therapy, representing a new trend in nanomedicine for cost-effective precision medicine. To date, most of the available theranostic nanoagents mainly utilize visible (400–700 nm) or near-infrared (NIR) light in the first NIR window (NIR-I, 700–900 nm) for optical molecular imaging and phototherapy, whereas fewer work have been exploited in the second NIR (NIR-II, 1000–1700 nm) window over the past few years.^[1] More recently, the NIR-II light has aroused rising interest in integrating cancer imaging and therapy applications.^[2] As compared to the visible or NIR-I light, NIR-II light exhibits intrinsic advantages of lesser photo scattering and higher maximum permissible exposure (MPE), resulting in increased penetra-


tion depth and improved sensitivity/efficacy for disease detection/therapy.^[3] Besides, another concern on the development of nanoagent for future clinical translation is the non-biodegradability and the potential long-term toxicity of nanoparticles. Therefore, the construction of noninvasive, biocompatible, and metabolizable tumor theranostic nanoplatfoms in NIR-II window is highly desired for their clinical translation.

Meanwhile, molecular imaging technologies also play a vital role in disease diagnosis and prognosis. For example, different biomedical imaging methods, such as magnetic resonance imaging (MRI),^[4] computed tomography (CT),^[5] and positron emission tomography (PET),^[6] have been extensively inspected for various preclinical and clinical applications. However, the downside of these imaging techniques is that the patients have to routinely suffer from the potential risk of exposure to radiation. Hence, the development of noninvasive functional imaging modalities are highly demanded for cancer early detection, which is also indispensable for personalized treatment

X. Men, Dr. Y. Liu, Dr. D. Gao, Prof. Z. Yuan
Cancer Center
Faculty of Health Sciences
Center for Cognitive and Brain Sciences
University of Macau
Macau 999078, China
E-mail: zhenyuan@um.edu.mo

F. Wang, Dr. H. Chen, X. Men, Prof. C. Wu
Department of Biomedical Engineering
Southern University of Science and Technology
Shenzhen, Guangdong 518055, China

Y. Yuan, Z. Zhang
State Key Laboratory on Integrated Optoelectronics
College of Electronic Science and Engineering
Jilin University
Changchun 130012, China

 The ORCID identification number(s) for the author(s) of this article can be found under <https://doi.org/10.1002/adfm.201909673>.

DOI: 10.1002/adfm.201909673

guidance to improve survival rates of cancer patients.^[7–9] In particular, photoacoustic (PA) imaging (PAI) is presently one of the most fast growing noninvasive imaging techniques, which enables high-resolution visualization of biological tissues for primary tumor detection, therapeutic monitoring, and the identification and assessment of metastatic lymph nodes.^[10–12]

More importantly, multifunctional absorbing nanomaterials can serve as exogenous nanoagents to improve PAI contrast for high-sensitivity disease detection.^[13,14] Interestingly, various categories of nanoagents have been well examined as contrast agents for enhanced PAI such as gold nanoparticles,^[15] carbon nanomaterials,^[16] and 2D nanoparticles.^[17] However, a core concern of the utilized nanoparticles is their poor biocompatibility, superficial penetration depth, and large sizes. By contrast, biocompatible organic nanoparticles including semiconducting polymer nanoparticles (SPNs) and semiconducting polymer dots (Pdots) have gained intensive research interests as PA contrast agents owing to their good biocompatibility, large absorption coefficient, tunable spectrum, excellent photostability, and abundant functional groups.^[18–21] Specifically, SPNs and Pdots generally exhibit a broad absorption spectrum with absorption peak in the NIR window.^[22] In addition, due to the high structural and functional flexibility, they can also serve as activatable imaging probes for PAI.^[23] Interestingly, compared with other categories of PA probes such as carbon and gold nanomaterials, SPNs usually show higher photostability and enhanced PA brightness.^[24]

In addition, due to the high NIR optical absorption and formidable nonradiative quantum efficiency, SPNs can also work as photothermal therapeutic reagent.^[25,26] SPNs with a photothermal effect in the NIR region have the ability to convert optical energy into heat that can ablate tumor cells for photothermal therapy (PTT).^[27,28] For example, our previous studies demonstrated that SPNs that have tunable NIR absorption peaks, can serve as promising photothermal agents and concurrent PA contrast agent for enhanced cancer theranostics.^[29] However, thanks to the inherent physicochemical properties, most of the constructed nanoparticles were with a diameter ranged from 10 to 200 nm, which significantly hindered their potential clinical application.^[30–33] Therefore, the degradation and discharge of nanoparticles from living body is still an unresolved issue and now under further investigation. Very recently, Liu's group inspected ultrasmall conjugated polymer nanoparticles (6 nm in diameter) for targeted cancer cell imaging,^[34] whereas Pu and co-workers demonstrated that NIR-II absorbing SPNs can be metabolizable with gradual clearance from living bodies after PAI.^[35] However, it is still a great challenge to develop a phototheranostic nanoplatform for cancer therapy with excellent biocompatibility, efficient body clearance, visibility on clinical imaging, and high photothermal conversion efficiency.

In this study, we design a type of novel ultrasmall and multifunctional Pdots via self-assembling of low-bandgap conjugated polymers and functional polymers under optimum conditions, which exhibits small particle sizes (4 nm in diameter), superior biocompatibility, high NIR-II absorption, and excellent photothermal conversion efficiency. The proof-of-concept application of Pdots is inspected in a mouse tumor model with i.v. injection for concurrent PAI and PTT. As displayed by the PAI results,

ultrasmall Pdots exhibit high-efficient tumor accumulation and rapid clearance capability. Meanwhile, in vivo PTT is also performed, in which we discover the used Pdots show a high efficiency tumor elimination effect under 1064 nm laser irradiation with 0.5 W cm⁻². Pdots constructed here should thus be a new category of theranostic agents for enhanced cancer diagnosis and treatment, which paves a new avenue for their potential clinical applications

2. Results and Discussion

2.1. Design, Preparation, and Characterizations of Ultrasmall Pdots

Diketopyrrolopyrrole-based semiconducting materials have been widely used in the field of optoelectronic and biological medical applications due to their tunable energy levels, excellent photostability, and large extinction coefficients. In this study, we designed and synthesized a novel semiconducting polymer, Poly([2,5-bis(2-decyltetradecyl)-2,5-dihydropyrrolo[3,4-c]pyrrole-1,4-dione-3,6-dithienyl]-co-[6-(2-ethylhexyl)-[1,2,5]thiadiazolo[3,4-f]benzotriazole-4,8-diyl]) (DPP-BTzTD, **Figure 1a**) by using the palladium-catalyzed Stille coupling polymerization (**Figure S1**, Supporting Information). In particular, the DPP-BTzTD polymers exhibit the electron donor-acceptor (D-A) alternating backbone, planar structures, and strong electron deficiency, resulting in broadband optical absorption in the NIR-II region. Gel permeation chromatography (GPC) measurements reveals that the number-averaged molecular weight (*M_n*) and weight-averaged molecular weight (*M_w*) of DPP-BTzTD is 7504 and 17263 Da, respectively, with a polydispersity index (PDI) of 2.30 (**Figure S2**, Supporting Information).

Ultrasmall Pdots was fabricated using a modified nanoreprecipitation method by self-assembling the polymer through hydrophilic and hydrophobic interactions. In a typical nanoreprecipitation, a mixture of conjugated polymer DPP-BTzTD and function polymer poly(styrene-co-maleic anhydride) (PSMA) in tetrahydrofuran (THF) was quickly injected into Triton X-100 solution under sonication in the ice-water solution for 10 min (**Figure 1b**). Triton X-100 solution was added to prevent the formation of large aggregates during the encapsulation process. The prolonged sonication time was essential to produce ultrasmall size and stable Pdots. During the process of heating to remove THF under nitrogen protection, Triton X-100 are also vital to prevent Pdots from further aggregation. After THF was removed, the mixture was dialyzed against the excess Triton X-100. Both Pdots prepared by different methods exhibit the spherical morphology as displayed by transmission electron microscope (TEM) (**Figure 1c,d**), while dynamic light scattering (DLS) reveals the average sizes of Pdots are 4 nm (S-Pdots) and 25 nm (L-Pdots) in diameters, respectively (**Figure 1e**). The Zeta potential results reveal that both the S-Pdots and L-Pdots possess a negative potential of -26 and -39 mV (**Figure 1f,g**). To make a better comparison between the S-Pdots and L-Pdots, the photophysical parameters of S-Pdots and L-Pdots are summarized and listed in **Table S1** (Supporting Information). In addition, the reproducibility of DLS and zeta potential measurements between the different batches of S-Pdots with the same condition is carefully inspected as well. It was discovered

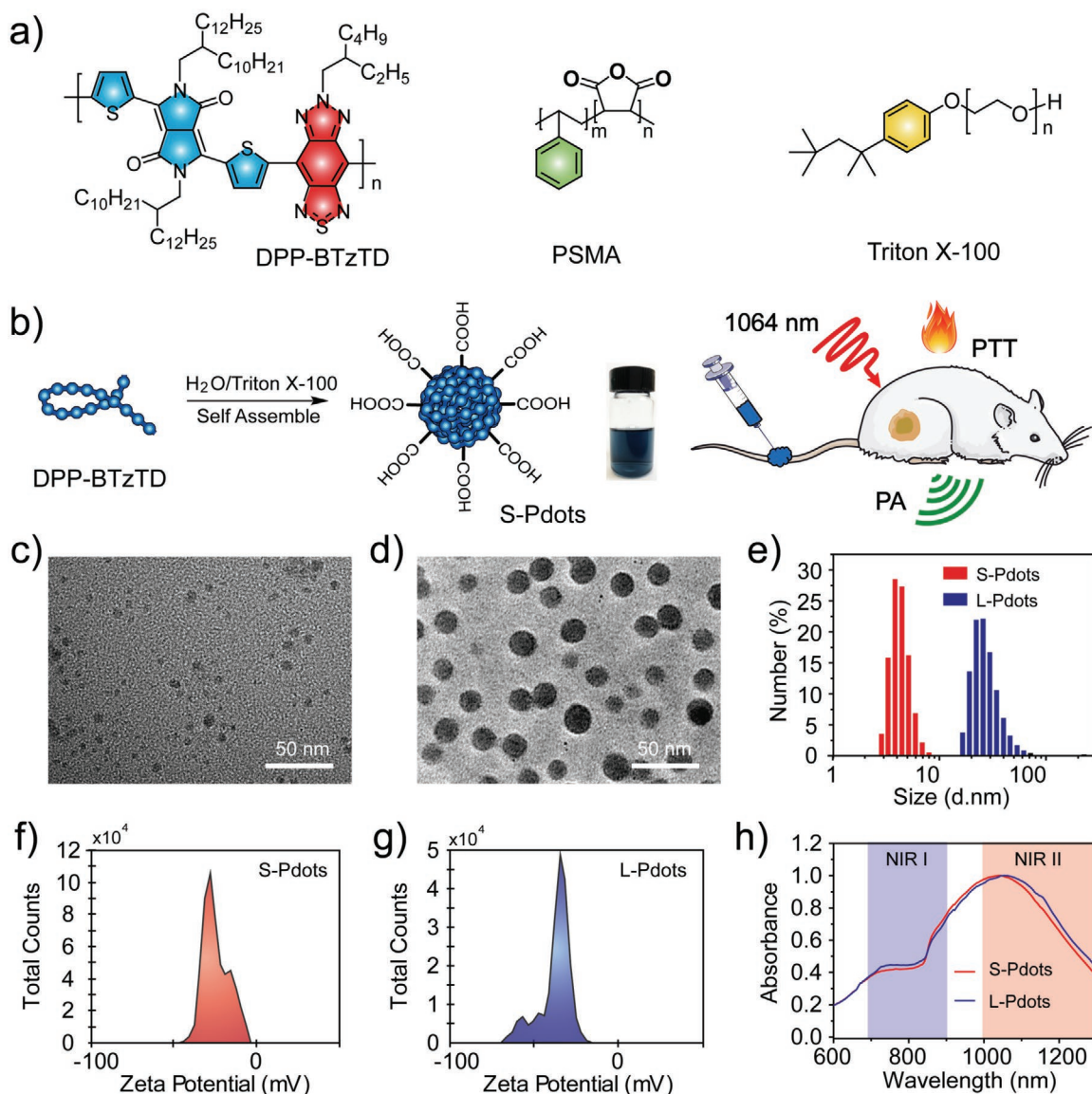


Figure 1. a) Chemical structural formula of the semiconducting polymer DPP-BTzTD, functional polymer PSMA, and Triton X-100. b) Schematic of DPP-BTzTD Pdots used for in vivo photoacoustic imaging (PA) guided photothermal therapy (PTT). c) Transmission electron microscope (TEM) image of DPP-BTzTD Pdots with averaged hydrodynamic particle diameter of 4 nm (S-Pdots). d) TEM image of DPP-BTzTD Pdots with corresponding sizes of 25 nm (L-Pdots). e) Representative dynamic light scattering (DLS) results of DPP-BTzTD S-Pdots (red) and L-Pdots (blue). f) Zeta potential results of S-Pdots. g) Zeta potential results of L-Pdots. h) NIR absorption spectra of DPP-BTzTD S-Pdots (red) and L-Pdots (blue).

from the analysis results in Figure S3 (Supporting Information) that S-Pdots exhibit excellent reproducibility between different batches. Importantly, as displayed in Figure S4 (Supporting Information), the DPP-BTzTD S-Pdots remain stable and clear without aggregation at room temperature after four weeks. Further analysis indicated that the S-Pdots also demonstrate good colloidal stability in biological buffer (Figure S5, Supporting Information).

Due to the high donor-acceptor (D-A) strength and planar alternating backbones (DPP as an electron-rich donor and BTzTD as an electron-deficient acceptor), DPP-BTzTD Pdots show a low bandgap and strong broad absorption between 800 and 1300 nm. Besides, photophysical properties of Pdots

are quantified underlying various physiological conditions. The S-Pdots and L-Pdots exhibit almost the same absorption spectra (Figure 1h), while the small diameter S-Pdots show an apparently blue-shifted, which is attributed to tighter bending and kinking of the polymer backbone and the overall decrease in conjugation length, as compared to the larger-diameter L-Pdots. Further, the mass extinction coefficient of DPP-BTzTD S-Pdots and L-Pdots is determined to be 52.5 and 53.6 $\text{L g}^{-1} \text{cm}^{-1}$ at 1064 nm, respectively, which is much higher than that of other recently reported nanoagents, e.g., 2.61 $\text{L g}^{-1} \text{cm}^{-1}$ for superparamagnetic polypyrrole nanocatalysts,^[36] 5.54 $\text{L g}^{-1} \text{cm}^{-1}$ for oxygen-deficient black titania, and 35.4 $\text{L g}^{-1} \text{cm}^{-1}$ for MXene nanosheets.^[37]

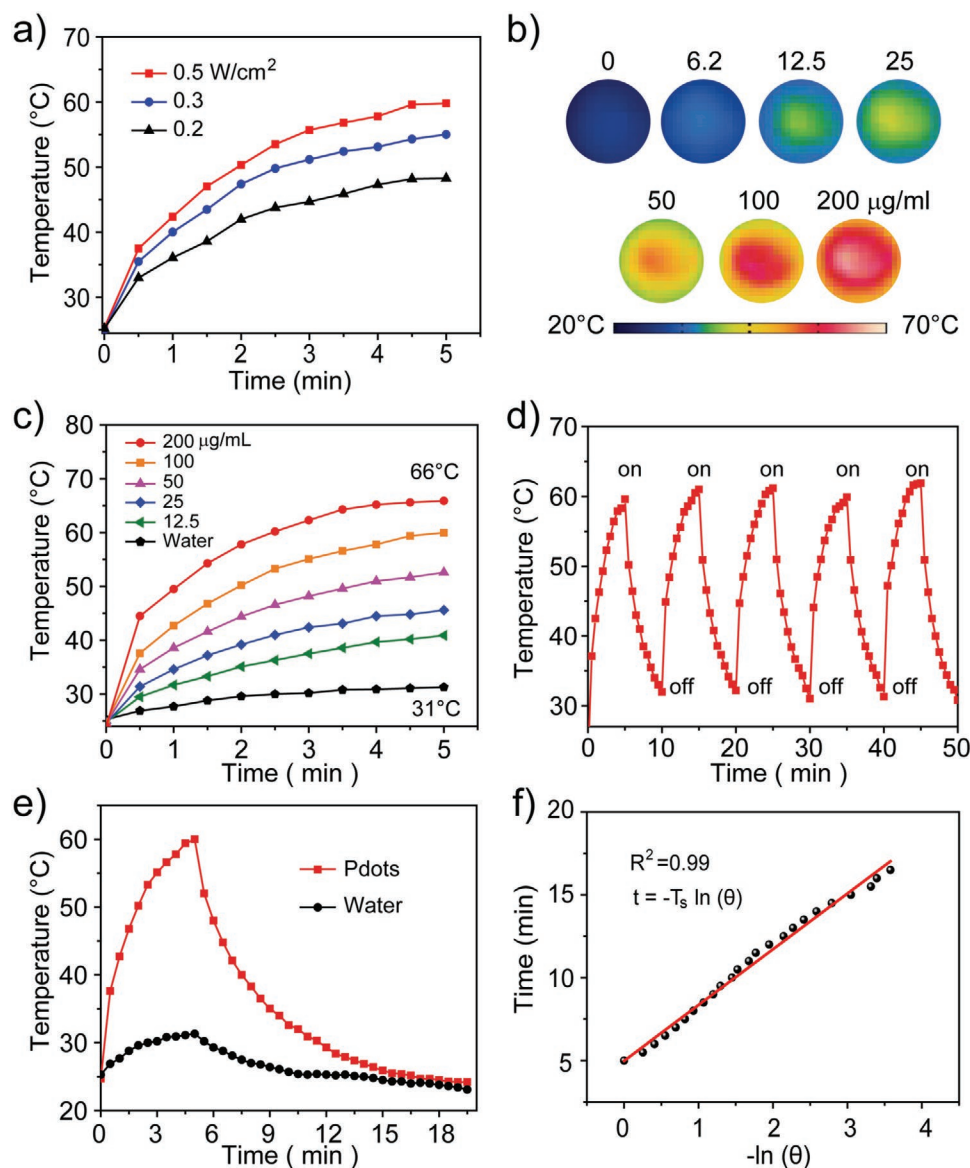


Figure 2. a) Photothermal heating curves of DPP-BTzTD S-Pdots dispersions ($100 \mu\text{g mL}^{-1}$) irradiated using a 1064 nm laser at varied power densities (0.2, 0.3, and 0.5 W cm^{-2}). b) Photothermal IR imaging of DPP-BTzTD S-Pdots solutions at different concentration (0, 6.2, 12.5, 25, 50, 100, and $200 \mu\text{g mL}^{-1}$) under 1064 nm laser irradiation at 0.5 W cm^{-2} for 5 min. c) The temperature evolution of DPP-BTzTD S-Pdots dispersions with various S-Pdots concentrations under 1064 nm laser irradiation. d) Temperature elevation of DPP-BTzTD S-Pdots dispersions under five on/off cycles. e) Photothermal performance of Pdots and water under 1064 nm laser irradiation for heating and cooling period. f) Linear time data versus $-\ln(\theta)$ obtained from the cooling period.

2.2. NIR-II Photothermal Properties of DPP-BTzTD Pdots

The developed DPP-BTzTD Pdots also demonstrate remarkable and broad absorption in the NIR-II window, which can serve as contrast agents for NIR-II PAI and concurrent photothermal agents for NIR-II PTT. To assess the photothermal properties of DPP-BTzTD Pdots, the temperature variation of S-Pdots solution is inspected *in vitro* at different power densities (0.2, 0.3, and 0.5 W cm^{-2}) under 1064 nm laser irradiation (Figure 2a). We discovered that S-Pdots solution shows strong laser-power-dependent photothermal effect. Figure 2b plots the infrared thermal images of S-Pdots solution at different concentrations

(0, 12.5, 25, 50, 100, and $200 \mu\text{g mL}^{-1}$) under continuous irradiation at a low power density of 0.5 W cm^{-2} , which is much lower than its maximum permissible exposure limit of 1 W cm^{-2} . When exposed for 5 min, rapid temperature increase is detected in S-Pdots solution even with a relatively low concentration of 25 mg mL^{-1} (Figure 2c). The temperature elevation of S-Pdots ($100 \mu\text{g mL}^{-2}$) can reach as high as $60 \text{ }^\circ\text{C}$. The temperature evolution reveals obvious concentration-dependent on the photothermal heating effect.

To evaluate the photothermal stability of DPP-BTzTD Pdots, the recyclable temperature evolution in the presence of S-Pdots is displayed in Figure 2d. The temperature evolution of S-Pdots

dispersions upon 1064 nm laser irradiation is monitored over time with reversible heating-cooling cycles (Figure 2e). During the five laser on/off cycles of NIR-II laser irradiation, no obvious change of the highest temperature is detected. In addition, the size and morphology of S-Pdots after PTT with continuous laser irradiation at 1064 nm for 30 min were provided in Figure S6 (Supporting Information). It was discovered that the size and morphology of S-Pdots show no obvious signal change before and after PPT, which demonstrates the outstanding photostability of S-Pdots. The photothermal conversion efficiency is another significant parameter for photothermal agents in quantification of the light to heat conversion ability. The S-Pdots solution is irradiated with 1064 nm laser at 0.5 W cm^{-2} for 5 min to reach a steady temperature state from 28 to 60 °C. Then the laser irradiation is stopped and the S-Pdots solution is cooled down to the ambient temperature. As a negative control, the pure water remains nearly unchanged in temperature from 28 to 32 °C. The photothermal conversion efficiency of S-Pdots and L-Pdots was 53.1% and 53.8%, respectively, which was quantified based on the previous method (Figure 2f and Equations S1–S9, Supporting Information).^[38] Interestingly, the high extinction coefficient, excellent photothermal stability, ultrahigh NIR-II photothermal conversion efficiency, and good biocompatibility of DPP-BTzTD Pdots also ensure their outstanding potential for PAI-guided PTT.

2.3. In Vitro Biocompatibility and PTT Effect of DPP-BTzTD Pdots

To assess the biocompatibility of DPP-BTzTD Pdots, 3-(4,5-dimethylthiazol-2-yl)-2,5-diphenyltetrazolium bromide (MTT) assay is performed to inspect the efficiency of killing cancer cells. The influence of S-Pdots on HeLa cervical carcinoma cells is examined by MTT assay. The results reveal that S-Pdots show no obvious toxic effects on HeLa cells after incubation for 24 and 48 h even at a high concentration of $100 \mu\text{g mL}^{-2}$. The cell viabilities are all above 90%, indicating the excellent biocompatibility of DPP-BTzTD Pdots (Figure 3a).

To further evaluate the PTT efficacy on living cells, the photothermal ablation of HeLa cancer cells is carried out using both the MTT assay and fluorescence imaging. Under 1064 nm laser irradiation, various concentrations of DPP-BTzTD S-Pdots as photothermal agent are added into the HeLa cells. The MTT results manifest that the HeLa cells viabilities are reduced with increased concentration of S-Pdots. For example, about 40% cells are killed with a low concentration ($25 \mu\text{g mL}^{-1}$) of S-Pdots, whereas about 90% HeLa cells are destroyed with $50 \mu\text{g mL}^{-1}$ S-Pdots at the laser power density of 0.5 W cm^{-2} (Figure 3b). In particular, when the concentration of S-Pdots is up to $100 \mu\text{g mL}^{-1}$, almost all of HeLa cells are ablated after irradiation for a very short time (5 min). Consequently, the cancer cells viability shows concentration-dependent relationship with DPP-BTzTD S-Pdots after NIR-induced PTT. In addition, confocal fluorescence imaging of calcein acetoxymethyl ester (calcein AM)/propidium iodide (PI) costained HeLa cells also confirms the high PTT ablation efficacy of S-Pdots (Figure 3c–h). By contrast, the cells treated with 1064 laser irradiation or S-Pdots alone are able to be alive. Hence, DPP-BTzTD S-Pdots can serve as an excellent photothermal agent for enhanced PTT in the presence of 1064 nm laser irradiation at a very low power density of 0.5 W cm^{-2} .

2.4. In Vivo PAI of Tumor

To inspect the PAI capability of DPP-BTzTD Pdots, in vitro phantom tests were performed, in which PA signal intensities were measured with increased concentrations of DPP-BTzTD S-Pdots from 50 to $200 \mu\text{g mL}^{-1}$ (Figure 4a). Figure 4b displayed that the PA intensity of S-Pdots ($R^2 = 0.99$) exhibited linear relationship with its concentration. In particular, the PA images of S-Pdots solution showed obvious concentration-dependent brightening effect, which is advantageous for quantitative PA analysis.

In addition, a 4T1 tumor-bearing nude mice model was established to examine the in vivo PAI performance of DPP-BTzTD Pdots. The mice were intravenously administrated with DPP-BTzTD S-Pdots, and then the PA signal intensity at tumor site was monitored at different time points with our home-made PAI system (Figure S7, Supporting Information). Figure 4c,d respectively plotted the generated in vivo PA images and corresponding PA signal intensities at the tumor site before and after the i.v. injection of S-Pdots under 1064 nm laser irradiation at different time points post-injection. We discovered that the PA images exhibited weak PA signals in the tumor region before the injection of the probe. However, after the tail-vein i.v. injection of DPP-BTzTD Pdots, the PAI contrast was enhanced, which demonstrated that Pdots can reach the tumor site through enhanced permeability and retention (EPR) effect. In particular, PA signals were clearly detected at 1 h post-injection of S-Pdots, which gradually increased till reached the peak at 2 h post-injection. And then PA signal intensities began to decrease till became stable at 24 h post-injection. For comparison, in vivo PAI was also performed using L-Pdots as contrast agent. As for L-Pdots, it was observed that PAI contrast was clearly improved at 1 h post-injection, and was further enhanced at 2 h. The PA signal intensity reached the peak at 4 h post-injection and then began to decrease slowly until became weak at 24 h post-injection. Interestingly, it is noted that the PA signal intensity of S-Pdots is higher than that of L-Pdots, which might be due to the large specific surface area and excellent light-capturing ability of S-Pdots. More importantly, compared to previous work that used traditional Pdots for PAI, the metabolic rate for the present study was significantly increased when S-Pdots serve as the PA contrast agent. Thus, DPP-BTzTD S-Pdots with the short tumor enrichment time and enhanced PAI capability offer us new candidates with a wide time window for PAI of tumor.

2.5. In Vivo Tumor PTT

The in vivo efficiency of PTT is also explored using the same xenograft model. All procedures were performed in compliance with the Animal Care and Use Committee of the University of Macau. The nude mice with tumor sizes of about 60 mm^3 were randomly divided into four groups ($n = 5$ per group), and then i.v. injection with S-Pdots at a dose of 2.0 mg kg^{-1} or the same volume of phosphate-buffered saline (PBS) were carried out. S-Pdots can be trapped in the tumor based on EPR effect. After 2 h post-injection, the tumor sites of mice were exposed to a 1064 nm laser with 0.5 W cm^{-2} for 5 min. The temperature

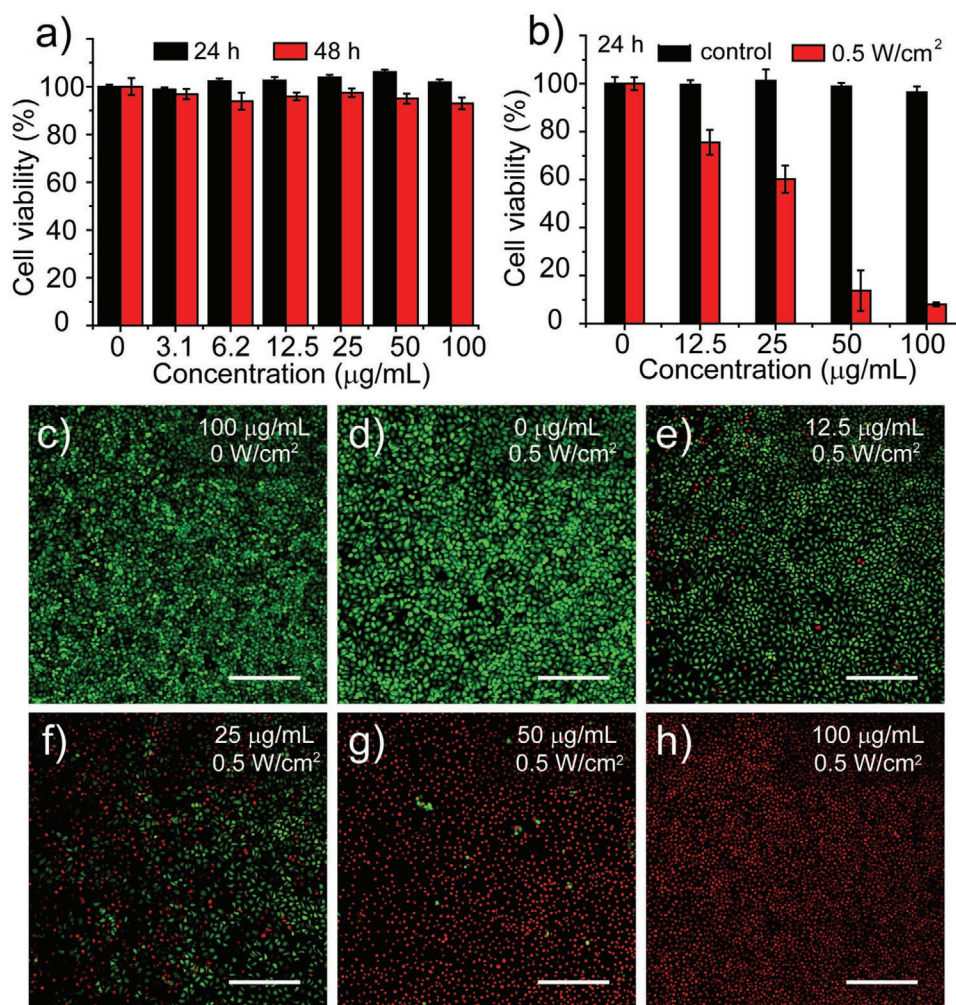


Figure 3. a) MTT assay of HeLa cells treated with DPP-BTzTD S-Pdots at various concentrations of 0, 3.1, 6.2, 12.5, 25, 50, and 100 $\mu\text{g mL}^{-1}$ for 24 or 48 h to assess the cells viability. Error bars denote the standard deviation ($n = 6$). b) Cell viability assessment of HeLa cells after incubation with different concentrations of DPP-BTzTD S-Pdots for 24 h: cells treated with irradiation (red) or without irradiation (black) using a 1064 nm NIR-II laser for 5 min. Error bars indicated standard deviation ($n = 6$). c) Confocal fluorescence image of HeLa cell stained by calcein AM and PI without irradiation, which were incubated with DPP-BTzTD S-Pdots (100 $\mu\text{g mL}^{-1}$). d–h) Confocal fluorescence images of live/dead HeLa cells incubated with DPP-BTzTD S-Pdots (0, 12.5, 25, 50, and 100 $\mu\text{g mL}^{-1}$) after irradiation by a 1064 nm laser at 0.5 W cm^{-2} for 5 min. Scale bar: 300 μm .

evolution under the irradiation treatment was characterized using an infrared thermal imager and those of the control groups injected with PBS were also monitored and measured (Figure 5a). As showed in the quantitative tumor temperature curves, the temperature of tumor sites that was injected with DPP-BTzTD Pdots rapidly reaches 56 °C for 5 min, which is high enough to ablate tumors. However, the temperature of tumor sites injected with PBS only increases to 38 °C within 5 min under the same irradiation condition (Figure 5b). As displayed in Figure 5c, NIR-II light with S-Pdots can inhibit the tumor growth.

More importantly, we discovered that the tumor after the injection of S-Pdots was eradicated for the PTT treatment group, which showed no recurrence within 2 weeks (Figure 5d). By contrast, the tumors from all control groups showed no trend of growth inhibition. In addition, the tumor size from the four groups were successfully measured every two days (Figure 5e). Further, as shown in Figure 5f, the body weight

changes of each group showed no obvious difference during the 14 days treatment period as well, indicating the low side toxic effect of treatment using S-Pdots with NIR-II irradiation. Therefore, our findings demonstrated that DPP-BTzTD S-Pdots exhibit excellent *in vivo* tumor therapeutic efficacy by PTT.

2.6. In Vivo Biodistribution and Blood Circulation Studies

The long-term biodistribution and toxicity of nanoagents remain to be the most important concern for their potential clinical applications. In this study, a histological examination was performed by hematoxylin and eosin (H&E) of the major organ slices (including the heart, liver, spleen, lung, and kidney) for the tumor-bearing mice. As shown in Figure 6a, the treated mice exhibited no appreciable damage to normal tissues, indicating that DPP-BTzTD Pdots have no observable side effect or toxicity to normal tissues with the tested dose.

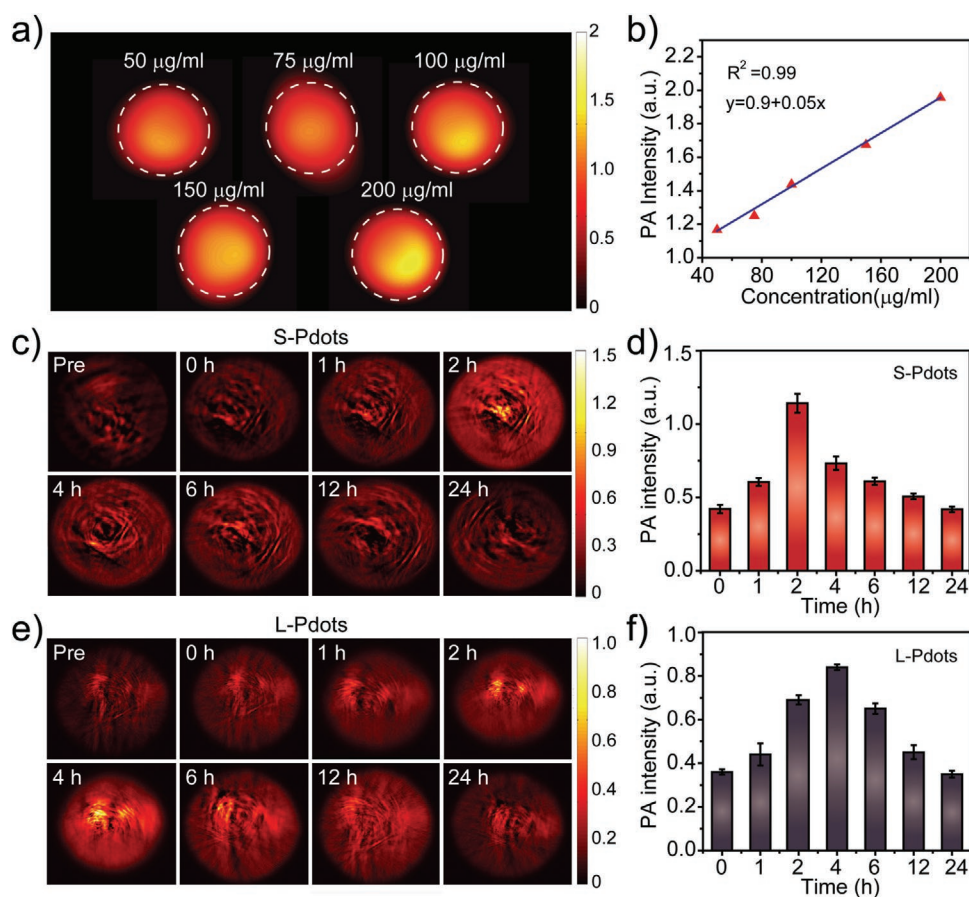


Figure 4. a) Photoacoustic images of DPP-BTzTD S-Pdots dispersions at various concentrations (50, 75, 100, 150, and 200 $\mu\text{g mL}^{-1}$). b) The corresponding photoacoustic signal intensities of DPP-BTzTD S-Pdots at various concentrations. c) In vivo PAI of nude mice after intravenous (i.v.) injection of DPP-BTzTD S-Pdots (at a dose of 2.0 mg kg^{-1} ; about 126–134 μL , 0.3 mg mL^{-1} , the volume varies depending on the weight of the mouse) at different time intervals (pre, 0, 1, 2, 4, 6, 12, and 24 h). d) The corresponding tumor photoacoustic signal intensity changes of mice after i.v. injection of DPP-BTzTD S-Pdots. Each data denote the mean \pm standard deviation from $n = 5$ animals. e) In vivo PAI of nude mice after i.v. injection of DPP-BTzTD L-Pdots at various time points. f) The corresponding tumor photoacoustic signal intensity changes of mice after i.v. injection of DPP-BTzTD L-Pdots at different time points. Each data denote the mean \pm standard deviation from $n = 5$ animals.

In addition, body clearance experiments were performed to inspect the in vivo kinetics and biodistribution of both S-Pdots and L-Pdots. To explore its accumulation effect, Pdots were doped with the silicon 2,3-naphthalocyanine bis(trihexylsilyloxy) dye (NIR 775) at a ratio of 1 wt% in order to visualize the Pdots distribution in different organs by using by fluorescence imaging.^[41] We also discovered that the size of as-prepared Pdots showed no obvious change as compared to that of Pdots before doping (Figure S8, Supporting Information). Meanwhile, the fluorescence emission of Pdots at 777 nm was detected (Figure S9, Supporting Information).

Further, the NIR775-doped Pdots were first injected into the nude mice intravenously via tail vein. And then the mice blood samples were collected and the major organs including the brain, the heart, the lung, the liver, the spleen, and the kidneys were excised and well visualized at designated time points by fluorescence imaging (Figure 6b and Figure S10, Supporting Information). Finally, it was discovered that the strong fluorescence signal of L-Pdots is mainly detected in liver, whereas that of S-Pdots can be identified in both liver and kidney at 6 h

post-injection. Interestingly, the fluorescence intensity of both S-Pdots and L-Pdots decreases gradually over time. However, the S-Pdots exhibit a quicker decrease than L-Pdots because the clearance of L-Pdots is largely through the biliary pathway while that of the S-Pdots can be excreted through both the biliary pathway and urethral system.^[34] In particular, the fluorescence intensity change of S-Pdots and L-Pdots in blood was also compared and displayed in Figure S11 (Supporting Information). The quick fluorescence intensity reduction of S-Pdots in blood further validates its fast body clearance as compared to that of L-Pdots.

Importantly, we also inspected the toxicity of DPP-BTzTD S-Pdots in blood. The tumor-bearing mice were intravenously injected with S-Pdots and then we collected the blood samples at 0 (before injection), 1, 7, and 14 d post-injection. Meanwhile, the blood routine indexes of the S-Pdots treated mice were respectively measured to compare with those of untreated groups. As shown in Figure 6c and Figure S12 (Supporting Information), the blood routine indexes include the white blood cells (WBC), red blood cells (RBC), hemoglobin (HGB),

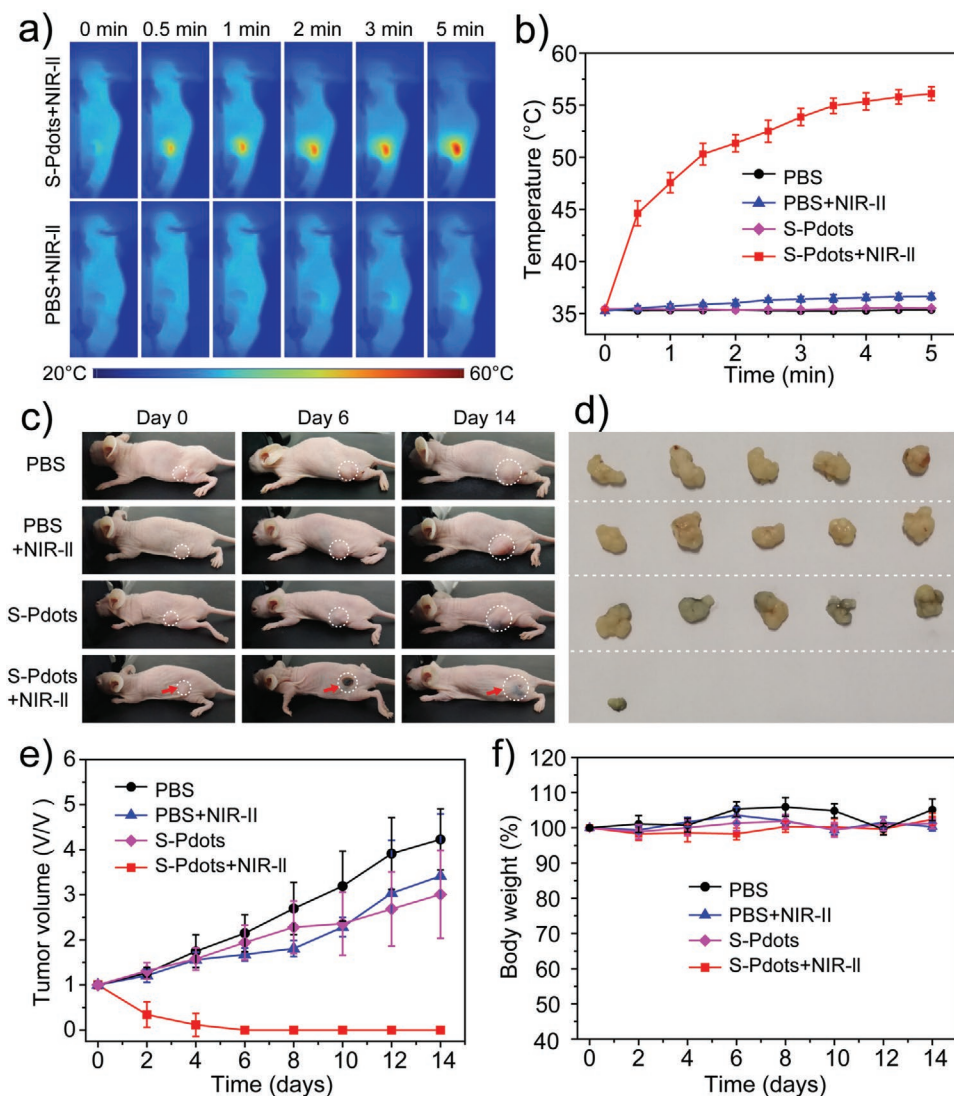


Figure 5. a) Photothermal IR thermal images of 4T1 tumor-bearing mice with DPP-BTzTD S-Pdots (at a dose of 2.0 mg kg^{-1} ; about $126\text{--}134 \mu\text{L}$, 0.3 mg mL^{-1} , the volume varies depending on the weight of the mouse) or PBS under the 1064 nm NIR-II laser irradiation at 0.5 W cm^{-2} . b) The temperature change of 4T1 tumor in vivo during PTT associated with four groups. Each data point denotes the mean \pm standard deviation from $n = 5$ animals. c) Representative 4T1 tumor-bearing mice photographs of four different groups after various treatments at different days. i) PBS; ii) PBS, NIR-II (1064 nm , 0.5 W cm^{-2} , 5 min); iii) S-Pdots; iv) S-Pdots, NIR-II (1064 nm , 0.5 W cm^{-2} , 5 min). d) Photographs of tumors after excision from the mice after corresponding treatment. e) The relative tumor volumes curves. Each data point denotes the mean \pm standard deviation from $n = 5$ animals. f) The body weight changes of mice after various treatments over 14 days. Each data point represents the mean \pm standard deviation from $n = 5$ animals.

platelet (PLT), mean corpuscular hemoglobin (MCH), mean corpuscular hemoglobin concentration (MCHC), mean platelet volume (MPV), and hematocrit (HCT). All detection indexes showed that they are normal for the treated group, suggesting that i.v. injection of S-Pdots has no major hepatotoxic effects and renal toxicity.

3. Conclusion

In summary, we have successfully constructed a phototheranostic nanoagent of DPP-BTzTD Pdts with the strong NIR-II absorption, excellent physiological stability, bright PA signals,

high photothermal conversion efficiency, and good biocompatibility. DPP-BTzTD Pdts with the ultrasmall size show high-effective cancer cell ablation capability in vitro and in vivo upon irradiation of NIR-II light together with rapid excretion through the renal filtration system. Based on enhanced bi-modal photothermal imaging and PAI, the structure and functional information of tumor can be effectively captured, indicating the specific targeting and efficient accumulation of DPP-BTzTD Pdts in tumor sites. Significant tumor ablation by PTT was also achieved after systemic administration of DPP-BTzTD Pdts, followed by 1064 nm laser irradiation. In addition, both blood circulation studies and histological examinations demonstrated that DPP-BTzTD Pdts show no toxicity to the mice

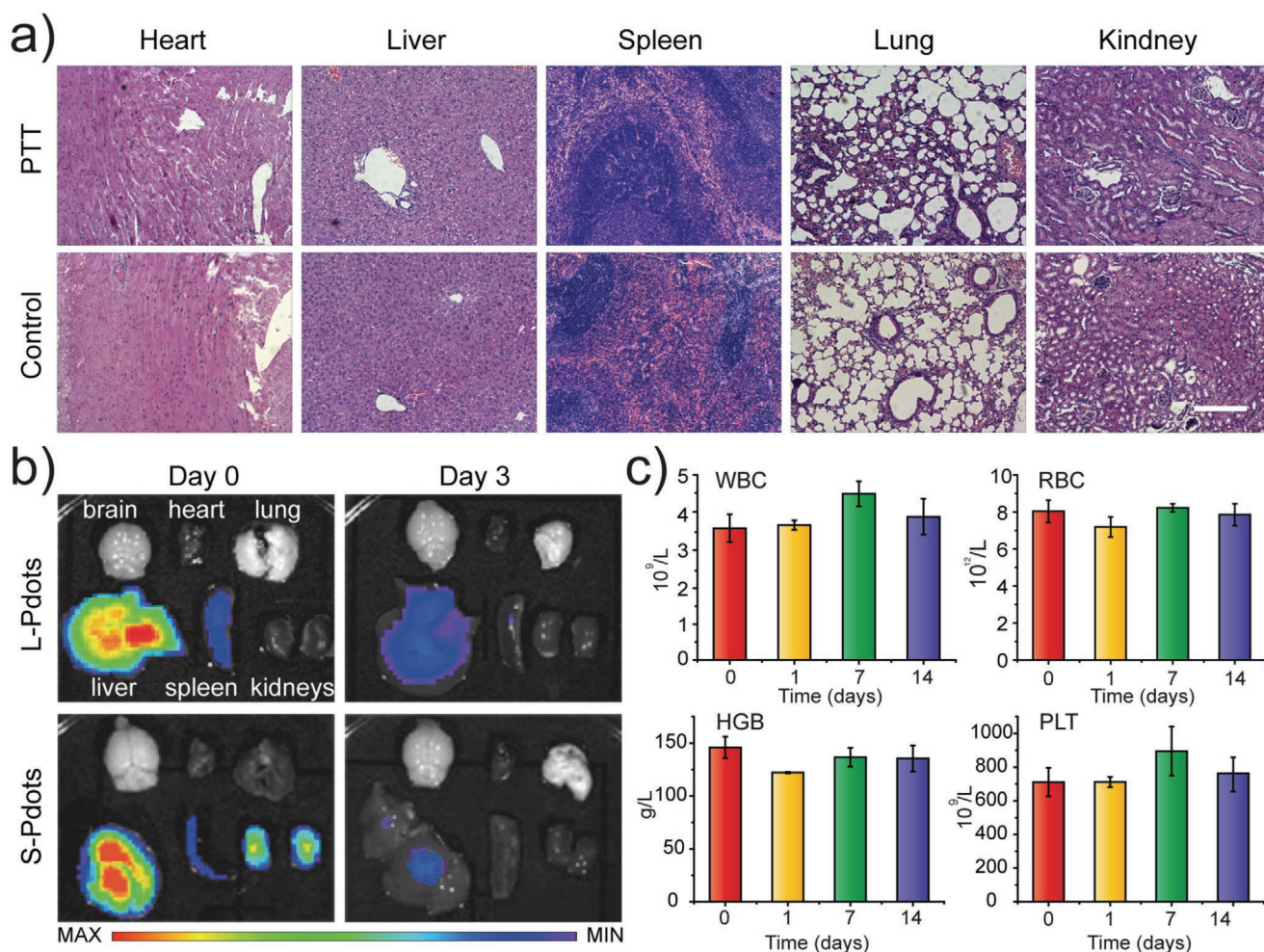


Figure 6. a) Hematoxylin and eosin (H&E) staining images of major organs from normal control mice and treated mice (S-Pdots, 1064 nm, 0.5 W cm⁻², 5 min) after treatment. Scale bar: 200 μ m. b) NIR fluorescence imaging of various organs (from the right to left and top to bottom: the brain, heart, lung, liver, spleen, and kidneys) dissected from mice after the i.v. injection of S-Pdots (at a dose of 2.0 mg kg⁻¹; about 126–134 μ L, 0.3 mg mL⁻¹, the volume varies depending on the weight of the mouse) at different time points post-injection (Day 0: 6 h, Day 3: 72 h; results at 1, 24, and 144 h provided in the Figure S10, Supporting Information). c) The blood routine indexes changes over time. (WBC: white blood cells, RBC: red blood cell, HGB: hemoglobin, and PLT: platelet; results of MCH: mean corpuscular hemoglobin, MCHC: mean corpuscular hemoglobin concentration, MPV: Mean platelet volume, and HCT: hematocrit provided in the Figure S12, Supporting Information). Each data value denotes the mean \pm standard deviation from $n = 5$ animals.

during the whole treatment period, which avoid the unnecessary side effects. Therefore, DPP-BTzTD Pdots show great promise for accurate diagnose and localizing tumor sites to guide efficient PTT. The developed theranostic nanoplatforms that incorporate enhanced diagnostic and therapeutic capability can confer upon these superior nanoprobes vast potentials in clinical translation of nanomedicine.

4. Experimental Section

Synthesis of Conjugated Polymer DPP-BTzTD: A new π -conjugated polymer was designed and synthesized by using the donor monomer DPP and acceptor monomer BTzTD. The conjugated polymers DPP-BTzTD was synthesized by the Stille polymerization,^[39] and the details are provided in the Supporting Information.

Preparation of DPP-BTzTD L-Pdots and S-Pdots: DPP-BTzTD L-Pdots was synthesized according to the previously reported nanoprecipitation

method by simple sonication.^[40] For a typical reprecipitation, a solution of conjugated polymer DPP-BTzTD (80 μ g mL⁻¹) and functional polymer PSMA (20 μ g mL⁻¹) was dissolved in fresh THF (for NIR775 doped Pdots, 0.8 μ g mL⁻¹ of NIR775 was also dissolved in this THF solution). And a 3 mL of the above mixture was rapidly dispersed into 10 mL ultrapure water under intense sonication. Then THF was evaporated from the dispersion using heating station under the nitrogen protection. Few aggregates were removed by a 0.22 μ m membrane filter. As for S-Pdots, while under the same conditions, by adding small amount of Triton X-100 (0.25 wt%) in the water solution and ultrasound in ice water bath for 10 min, the preparation produced the ultrasmall size DPP-BTzTD S-Pdots. Finally, Triton X-100 can be easily removed by dialysis for 48 h.

Cytotoxicity Assays: The activities of HeLa cervical cells in vitro was evaluated using 3-[4,5-dimethylthiazol-2-yl]-2,5-diphenyltetrazolium bromide (MTT) assays. HeLa cells were seeded in 96 well plates (Costar, Chicago, IL, USA) and grown to 80%. Then the HeLa cells were further incubated with DPP-BTzTD S-Pdots with different concentrations for 24 and 48 h, respectively. Later on, 20 μ L of MTT solution at 5 mg mL⁻¹ was added into each well, and then the samples were incubated for an additional 4 h. Subsequently, 150 μ L of dimethyl sulfoxide (DMSO) was

added into each well plate. Further, the optical density was measured using a microplate reader (BioTek Cytation 3). The activities of HeLa cells were calculated by using the following equation

$$\text{Cell viability (\%)} = \frac{\overline{A}_t}{\overline{A}_c} \times 100\% \quad (1)$$

in which \overline{A}_t and \overline{A}_c is the mean absorbance of the treatment and control group, respectively.

Tumor Mouse Model: All mice procedures were approved by the Animal Care and Use Committee of University of Macau. Female nude mice were obtained from Beijing HFK Bioscience Co., Ltd.. The 4T1 tumor model was developed by subcutaneous injection of 4T1 mammary carcinoma cells with an amount of 7×10^7 cells (50 μL in PBS) into the dorsal area of each 6-week-old female nude mouse.

PAI: 4T1-bearing female nude mice were administered with DPP-BTzTD S-Pdots or PBS through i.v. injection. PAI was carried out after the i.v. injection at different time points. The PA images were generated with a holder designed specifically system at a wavelength of 1064 nm in the University of Macau.

PTT: For the in vitro PTT experiments, HeLa cervical cells were incubated in 6 well cell culture plates at 2×10^4 cells well⁻¹ for 6 h. And then various mass concentrations of DPP-BTzTD S-Pdots solution were added into the HeLa cells that were further incubated for 24 h. Subsequently, HeLa cells were illuminated with a 1064 nm laser at a power density of 0.5 W cm^{-2} for 5 min, which were further incubated for additional 12 h. By contrast, the control groups were incubated in darkness at 37 °C in an atmosphere containing 5% CO₂ for the same period of time. Cell viabilities were then measured using the same method with 96 well plates as cytotoxicity assay. For fluorescence imaging, the HeLa cells after exposure with a 1064 nm laser at 0.5 W cm^{-2} for 5 min were then stained using a calcein-AM and PI double-staining agent, and then imaged using a confocal scanning microscope (Olympus FV1000). For the in vivo PTT experiments, T41-bearing nude mice were randomized into four different groups after the tumors reached $\approx 60 \text{ mm}^3$ ($n = 5$ per group): i) PBS; ii) PBS, irradiated with an NIR-II laser of 1064 nm at 0.5 W cm^{-2} for 5 min; iii) DPP-BTzTD S-Pdots; iv) DPP-BTzTD S-Pdots, irradiated with an NIR-II laser of 1064 nm at 0.5 W cm^{-2} for 5 min. The temperature changes were monitored using a SC300 infrared camera (Fluke TiR, USA). The volume of tumor was calculated by the following equation

$$\text{Volume} = \frac{1}{2} \times \text{Length} \times \text{Width}^2 \quad (2)$$

Body Clearance: NIR775 doped S-Pdots and L-Pdots were intravenously injected into nude mice at a dose of 2.0 mg kg^{-1} (about 126–134 μL , 0.3 mg mL^{-1} , the volume varies depending on the weight of the mouse) in two groups ($n = 10$ per group), respectively. At designated time point (1, 6, 24, 72, and 144 h), the blood samples were collected from the venous sinus and centrifuging to obtain serum. Two mice in each group were sacrificed to extract the brain, heart, lung, liver, spleen, and kidneys. The fluorescence intensity of various organs were imaged using IVIS Lumina XR III system for ex vivo fluorescence imaging.

Data Analysis: Results were expressed as the Mean \pm SD unless stated otherwise. The PA data were analyzed using Matlab software. Photothermal IR images were analyzed using SmartView software. The fluorescence data were measured by ROI analysis using Living Image Software for IVIS Lumina XR III system.

Supporting Information

Supporting Information is available from the Wiley Online Library or from the author.

Acknowledgements

The authors acknowledge financial support from grants FDCT 0011/2018/A1 and FDCT 025/2015/A1 from the Macau government and grants MYRG2014-00093-FHS, MYRG 2015-00036-FHS, MYRG2016-00110-FHS, and MYRG2018-00081-FHS from the University of Macau. This work was also financially supported by the grants from NSFC (No. 81771930), National Key R&D Plan of China (No. 2018YFB0407200), and Shenzhen Science and Technology Innovation Commission (No. JCYJ20170307110157501).

Conflict of Interest

The authors declare no conflict of interest.

Author Contributions

X.M., F.W., and H.C. contributed equally to this work. X.M., H.C., and Z.Y. conceived the study and wrote the majority of the manuscript content; X.M., F.W., and H.C. performed the in vitro and in vivo PTT experiments; Y.L. and X.M. performed PAI experiments. F.W. and X.X.M. performed body clearance experiments; H.C. synthesized and provided DPP-BTzTD. Y.Y. and Z.Z. helped with histological studies; D.G. and C.W. were involved in discussions. All of the authors reviewed and contributed to the manuscript.

Keywords

photoacoustic imaging, photothermal therapy, polymer dots, second near-infrared window, semiconducting polymers

Received: November 19, 2019

Revised: March 13, 2020

Published online: April 27, 2020

- [1] Q. Q. Miao, K. Y. Pu, *Adv. Mater.* **2018**, *30*, 1801778.
- [2] A. M. Smith, M. C. Mancini, S. M. Nie, *Nat. Nanotechnol.* **2009**, *4*, 710.
- [3] S. Q. He, J. Song, J. L. Qu, Z. Cheng, *Chem. Soc. Rev.* **2018**, *47*, 4258.
- [4] K. J. Cai, M. Haris, A. Singh, F. Kogan, J. H. Greenberg, H. Hariharan, J. A. Detre, R. Reddy, *Nat. Med.* **2012**, *18*, 302.
- [5] Y. Cheng, Y. Chang, Y. L. Feng, H. Jian, Z. H. Tang, H. Y. Zhang, *Angew. Chem., Int. Ed.* **2018**, *57*, 246.
- [6] D. Q. Chen, D. Z. Yang, C. A. Dougherty, W. F. Lu, H. W. Wu, X. R. He, T. Cai, M. E. Van Dort, B. D. Ross, H. Hong, *ACS Nano* **2017**, *11*, 4315.
- [7] S. Heskamp, W. Hobo, J. D. M. Molkenboer-Kuenen, D. Olive, W. J. G. Oyen, H. Dolstra, O. C. Boerman, *Cancer Res.* **2015**, *75*, 2928.
- [8] F. Zhang, J. B. Cao, X. Chen, K. Yang, L. Zhu, G. F. Fu, X. L. Huang, X. Y. Chen, *Theranostics* **2015**, *5*, 1444.
- [9] H. Wan, H. Du, F. Wang, H. Dai, *Adv. Funct. Mater.* **2019**, *29*, 1900566.
- [10] M. H. Zhang, H. S. Kim, T. F. Jin, A. Yi, W. K. Moon, *Biomed. Opt. Express* **2016**, *7*, 1920.
- [11] Z. Yang, R. Tian, J. J. Wu, Q. L. Fan, B. C. Yung, G. Niu, O. Jacobson, Z. T. Wang, G. C. Yu, W. Huang, J. B. Song, X. Y. Chen, *ACS Nano* **2017**, *11*, 4247.
- [12] S. Mallidi, K. Watanabe, D. Timerman, D. Schoenfeld, T. Hasan, *Theranostics* **2015**, *5*, 289.
- [13] L. H. V. Wang, S. Hu, *Science* **2012**, *335*, 1458.

- [14] X. D. Wang, Y. J. Pang, G. Ku, X. Y. Xie, G. Stoica, L. H. V. Wang, *Nat. Biotechnol.* **2003**, *21*, 803.
- [15] S. Mallidi, T. Larson, J. Tam, P. P. Joshi, A. Karpouk, K. Sokolov, S. Emelianov, *Nano Lett.* **2009**, *9*, 2825.
- [16] A. De La Zerda, C. Zavaleta, S. Keren, S. Vaithilingam, S. Bodapati, Z. Liu, J. Levi, B. R. Smith, T. J. Ma, O. Oralkan, Z. Cheng, X. Y. Chen, H. J. Dai, B. T. Khuri-Yakub, S. S. Gambhir, *Nat. Nanotechnol.* **2008**, *3*, 557.
- [17] X. X. Qian, S. D. Shen, T. Liu, L. Cheng, Z. Liu, *Nanoscale* **2015**, *7*, 6380.
- [18] K. Y. Pu, A. J. Shuhendler, J. V. Jokerst, J. G. Mei, S. S. Gambhir, Z. N. Bao, J. H. Rao, *Nat. Nanotechnol.* **2014**, *9*, 233.
- [19] J. C. Li, K. Y. Pu, *Chem. Soc. Rev.* **2019**, *48*, 38.
- [20] B. Guo, Z. H. Sheng, Kenry, D. H. Hu, X. W. Lin, S. D. Xu, C. B. Liu, H. R. Zheng, B. Liu, *Mater. Horiz.* **2017**, *4*, 1151.
- [21] C. Wu, D. T. Chiu, *Angew. Chem., Int. Ed.* **2013**, *52*, 3086.
- [22] Y. Y. Jiang, P. K. Upputuri, C. Xie, Y. Lyu, L. L. Zhang, Q. H. Xiong, M. Pramanik, K. Y. Pu, *Nano Lett.* **2017**, *17*, 4964.
- [23] J. L. Geng, C. Y. Sun, J. Liu, L. D. Liao, Y. Y. Yuan, N. Thakor, J. Wang, B. Liu, *Small* **2015**, *11*, 1603.
- [24] Y. Y. Jiang, K. Y. Pu, *Small* **2017**, *13*, 1700710.
- [25] T. T. Sun, J. H. Dou, S. Liu, X. Wang, X. H. Zheng, Y. P. Wang, J. Pei, Z. G. Xie, *ACS Appl. Mater. Interfaces* **2018**, *10*, 7919.
- [26] J. F. Zhang, C. X. Yang, R. Zhang, R. Chen, Z. Y. Zhang, W. J. Zhang, S. H. Peng, X. Y. Chen, G. Liu, C. S. Hsu, C. S. Lee, *Adv. Funct. Mater.* **2017**, *27*, 1605094.
- [27] Z. Y. Cao, L. Z. Feng, G. B. Zhang, J. X. Wang, S. Shen, D. D. Li, X. Z. Yang, *Biomaterials* **2018**, *155*, 103.
- [28] Yang, T., Liu, L., Deng, Y. B., Guo, Z. Q., Zhang, G. B., Ge, Z. S., Ke, H. T., Chen, H. B., *Adv. Mater.* **2017**, *29*, 1700487.
- [29] H. B. Chen, J. Zhang, K. W. Chang, X. J. Men, X. F. Fang, L. B. Zhou, D. L. Li, D. Y. Gao, S. Y. Yin, X. J. Zhang, Z. Yuan, C. F. Wu, *Biomaterials* **2017**, *144*, 42.
- [30] K. W. Chang, Z. H. Liu, X. F. Fang, H. B. Chen, X. J. Men, Y. Yuan, K. Sun, X. J. Zhang, Z. Yuan, C. F. Wu, *Nano Lett.* **2017**, *17*, 4323.
- [31] X. Z. Chen, R. Q. Li, Z. H. Liu, K. Sun, Z. Z. Sun, D. N. Chen, G. X. Xu, P. Xi, C. F. Wu, Y. J. Sun, *Adv. Mater.* **2017**, *29*, 1604850.
- [32] T. Senthilkumar, L. Y. Zhou, Q. Gu, L. B. Liu, F. T. Lv, S. Wang, *Angew. Chem., Int. Ed.* **2018**, *57*, 13114.
- [33] H. B. Chen, X. F. Fang, Y. Jin, X. Hu, M. Yin, X. J. Men, N. Chen, C. H. Fan, D. T. Chiu, Y. Z. Wan, C. F. Wu, *Small* **2018**, *14*, 1800239.
- [34] G. X. Feng, J. Liu, R. R. Liu, D. Mao, N. Tomczak, B. Liu, *Adv. Sci.* **2017**, *4*, 1600407.
- [35] Y. Y. Jiang, P. K. Upputuri, C. Xie, Z. L. Zeng, A. Sharma, X. Zhen, J. C. Li, J. G. Huang, M. Pramanik, K. Y. Pu, *Adv. Mater.* **2019**, *31*, 1808166.
- [36] W. Feng, X. G. Han, R. Y. Wang, X. Gao, P. Hu, W. W. Yue, Y. Chen, J. L. Shi, *Adv. Mater.* **2019**, *31*, 1805919.
- [37] H. Lin, S. S. Gao, C. Dai, Y. Chen, J. L. Shi, *J. Am. Chem. Soc.* **2017**, *139*, 16235.
- [38] D. K. Roper, W. Ahn, M. Hoepfner, *J. Phys. Chem. C* **2007**, *111*, 3636.
- [39] H. B. Chen, F. Wang, M. Y. Liu, M. D. Qian, X. J. Men, C. F. Yao, L. Xi, W. P. Qin, G. S. Qin, C. F. Wu, *Laser Photonics Rev.* **2019**, *13*, 1800326.
- [40] L. H. Feng, C. L. Zhu, H. X. Yuan, L. B. Liu, F. T. Lv, S. Wang, *Chem. Soc. Rev.* **2013**, *42*, 6620.
- [41] Jiang, Y., Li, J., Zhen, X., Xie, C., Pu, K., *Adv. Mater.* **2018**, *30*, 1705980.